

# Ni Doped CoS<sub>2</sub> as Cathode Catalysts with Enhanced Performances for Lithium–Oxygen Batteries

Cheng Jian, Zhiyong Yu\*, Kang Chen, Hanxing Liu

School of Materials Science and Engineering, Wuhan University of Technology,  
Wuhan, 430070, P. R. China

\*E-mail: [yuzhiyong@whut.edu.cn](mailto:yuzhiyong@whut.edu.cn)

Received: 18 March 2022 / Accepted: 29 April 2022 / Published: 6 June 2022

In this paper, Ni doped CoS<sub>2</sub> catalysts were synthesized via a one-step hydrothermal method. The SEM images showed that Ni doping played an important role in determining the primary particles size of the samples, which decreased firstly and then increased with increasing Ni contents. The electrocatalytic activities of Ni<sub>x</sub>Co<sub>1-x</sub>S<sub>2</sub> were also significantly influenced by Ni addition, in which Ni<sub>0.5</sub>Co<sub>0.5</sub>S<sub>2</sub> evinced the best catalytic performances. The lithium-oxygen cells with bimetallic catalysts demonstrated higher initial charge-discharge capacities, better rate capabilities and improved cycling performances. The initial discharge specific capacity for the cell with Ni<sub>0.5</sub>Co<sub>0.5</sub>S<sub>2</sub> could reach up to 4878, 3400 and 2244 mAh/g under 100, 200 and 400 mA/g, respectively. In addition, the lithium-oxygen cell containing Ni<sub>0.5</sub>Co<sub>0.5</sub>S<sub>2</sub> catalyst could be cycled 67 times with a limited capacity of 500 mAh/g under 100 mA/g. The improved electrochemical performances could contribute to the synergistic effects of the Co and Ni ions.

**Keywords:** Lithium-oxygen batteries, hydrothermal, bifunctional catalyst, bimetallic disulfide

## 1. INTRODUCTION

Lithium-oxygen batteries, as promising energy storage devices, have aroused widespread research interest as a consequence of their low costs and high energy densities to confront the shortage of fossil fuels and environmental problems [1-4]. Nevertheless, the sluggish reaction rates and low energy efficiency of oxygen reduction/evolution reactions (ORR/OER) severely hamper their applications [5, 6]. The exploration of efficient catalysts with bifunctional catalytic activity has been considered as one of the encouraging ways to address the above challenges [7-9].

Some noble metal based catalysts, like Pt and IrO<sub>2</sub>, are widely known for their superior ORR/OER activities, but the rareness and high cost of them seriously restrict their extensive applications [10, 11]. Recently, metal disulfides have been investigated as potential electrocatalysts

owing to their low cost, high earth abundance and prominent catalytic efficiency [12-15]. Especially, pyrite-type cobalt disulfide ( $\text{CoS}_2$ ) has been extensively explored as an electrocatalyst in various fields, such as the hydrogen evolution reaction (HER) [16, 17], dye-sensitized solar cells [18, 19] and lithium-oxygen batteries [20, 21] on account of its metal-like conductivity, good stability and excellent catalytic activity. On the other hand, the nickel sulfides, such as  $\text{NiS}$  [22],  $\text{Ni}_3\text{S}_2$  [23] and  $\text{NiS}_2$  [24], have also been studied as electrocatalysts, in which  $\text{NiS}_2$  with a bandgap of  $\sim 0.4$  eV has risen as an important candidate because of its theoretically high catalytic activity for HER, ORR and OER [25-27]. However, monometallic sulfides are not desirable candidates for electrocatalytic applications because their catalytic activities still function less effectively than noble metal-based catalysts. Compared with monometallic sulfides, bimetallic sulfides exhibit better catalytic performances due to higher electrical conductivity, richer redox reaction sites and adjustable absorption/desorption energies [28-30]. In view of the above merits, bimetallic sulfides are recently attracting growing interest as bifunctional electrocatalysts for lithium-oxygen batteries (LOBs) [31-33].

Cobalt and nickel are adjacent transition metal elements. The ion radius of  $\text{Ni}^{2+}$  is close to that of  $\text{Co}^{2+}$ . In addition,  $\text{CoS}_2$  and  $\text{NiS}_2$  belong to similar pyrite structure with a space group of Pa-3. Given the similarity in the crystal structure and ionic radius, a solid solution of  $\text{Ni}_x\text{Co}_{1-x}\text{S}_2$  is expected to form, which will be beneficial for optimizing the electrochemical catalytic activities by adjusting the compositions of active materials, tuning the electron structures and regulating multi-functional active sites of active materials. Nonetheless, the study of  $\text{Ni}_x\text{Co}_{1-x}\text{S}_2$  as electrocatalysts for LOBs has never been reported so far. Herein, a series of  $\text{Ni}_x\text{Co}_{1-x}\text{S}_2$  with  $x$  from 0 to 1 were prepared using a hydrothermal method. For the first time, a comparison of the electrocatalytic activities of bimetallic disulfides compared to the corresponding monometallic disulfides  $\text{CoS}_2$  and  $\text{NiS}_2$  was investigated in this work. The impacts of substituting cobalt ions with nickel ions on the electrochemical performances of LOBs were also addressed here. It can be found that significantly improved electrochemical performances of the lithium-oxygen cells were achieved by using the bimetallic catalysts.

## 2. EXPERIMENTAL SECTION

### 2.1 Samples preparation

The  $\text{Ni}_x\text{Co}_{1-x}\text{S}_2$  ( $x = 0, 0.25, 0.5, 0.75$  and  $1$ ) catalysts were prepared through a one-step hydrothermal approach (see Figure 1). Typically, 2.5 mmol ethylene-diamine-teraacetic acid disodium salt (EDTA-2Na) was firstly dissolved into 80 mL deionized water, after which a total of 0.01 mol of  $\text{Ni}(\text{NO}_3)_2 \cdot 6\text{H}_2\text{O}$  and  $\text{CoCl}_2 \cdot 6\text{H}_2\text{O}$  were added at the designed molar ratio. Then, 0.025 mol  $\text{Na}_2\text{S}_2\text{O}_3 \cdot 5\text{H}_2\text{O}$  was dissolved into the aforementioned solution under stirring. Thereafter, the mixing substances were placed into a 100 mL autoclave and held for 36 hours under  $180^\circ\text{C}$ . After naturally cooling down, the products were rinsed several times with deionized water,  $\text{CS}_2$  and absolute ethanol before being dried in vacuum for 12 hours under  $80^\circ\text{C}$ . The obtained samples were labeled as  $\text{CoS}_2$ ,  $\text{Ni}_{0.25}\text{Co}_{0.75}\text{S}_2$ ,  $\text{Ni}_{0.5}\text{Co}_{0.5}\text{S}_2$ ,  $\text{Ni}_{0.75}\text{Co}_{0.25}\text{S}_2$  and  $\text{NiS}_2$ .

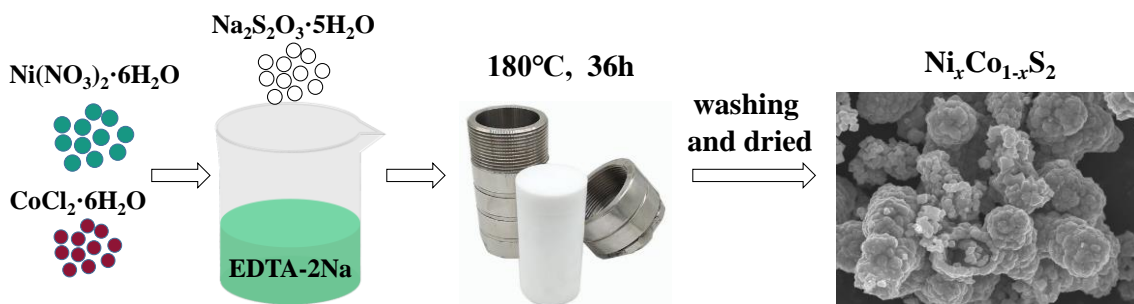


**Figure 1.** Schematic illustration of preparing the  $\text{Ni}_x\text{Co}_{1-x}\text{S}_2$  samples

## 2.2 Material characterizations

The phase structure analysis of  $\text{Ni}_x\text{Co}_{1-x}\text{S}_2$  was performed on X-ray diffraction (XRD, X'Pert PRO) with Cu  $K\alpha$  over  $2\theta$  range of  $20\text{--}80^\circ$ . Scanning electron microscopy (SEM, Zeiss Ultra Plus) was applied to examine the morphology of the products. The relative proportions of Co and Ni elements in the synthetic materials were determined using an inductively coupled plasma emission spectrometer (ICP, Prodigy 7). X-ray photoelectron spectroscopy testing (XPS, ESCALAB 250Xi) was carried out to investigate the surface chemical states.

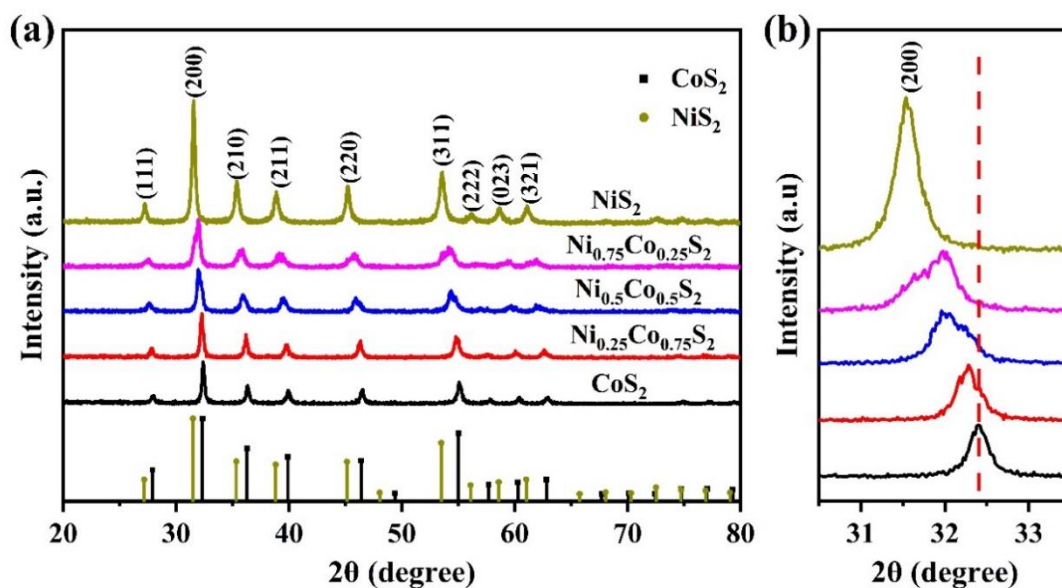
## 2.3 Electrochemistry measurements

The LOBs were assembled into coin-cells (CR2032) in an Argon-filled glove box, containing the  $\text{O}_2$  cathode, lithium foil anode, the electrolyte (1 mol/L LiTFSI in DMSO) and the separator (glass fiber). To prepare the  $\text{O}_2$  cathode, the as-synthesized catalysts, Super P and polyvinylidene fluoride (PVDF) were blended in N-methyl-2-pyrrolidone (NMP) to prepare an ink with a mass ratio of 27: 63: 10. The ink was then coated evenly onto a Ni mesh (diameter = 15 mm) and dried at  $100^\circ\text{C}$  before usage. The LOBs' discharge/charge capacities and cycling performances were recorded on LAND-CT2001A. The cyclic voltammetry (CV) measurements were obtained from 2.0 V to 4.5 V at 1 mV/s on CHI660B. All of the tests were conducted under room temperature.

## 3. RESULTS AND DISCUSSION

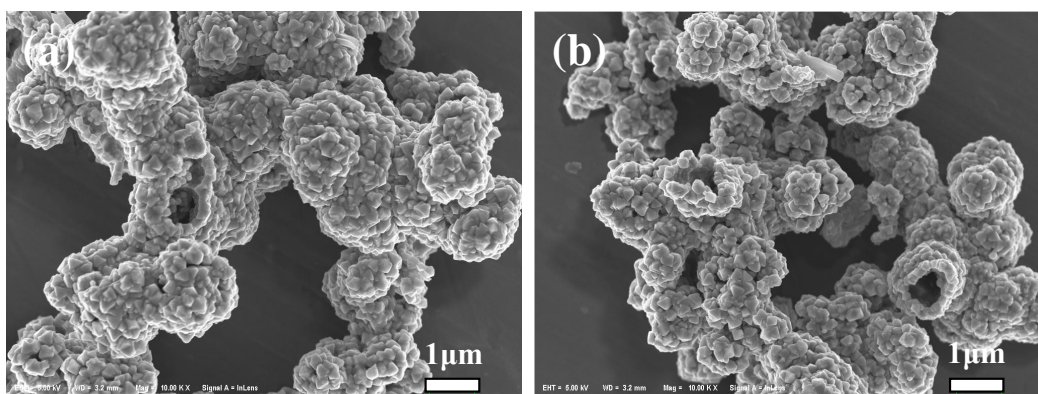
Figure 2a displays the XRD patterns of  $\text{Ni}_x\text{Co}_{1-x}\text{S}_2$  with  $x$  from 0 to 1 and the standard diffraction peaks of  $\text{CoS}_2$  (PDF#41-1471) and  $\text{NiS}_2$  (PDF#65-3325). The diffraction peaks of the sample without Ni correspond well with  $\text{CoS}_2$ , whereas those of the sample without Co can be well indexed as  $\text{NiS}_2$ . The partial magnification of the (200) peaks is exhibited in Figure 2b. Obviously, with the increase of Ni doping content, the diffraction peaks gradually shift to lower angles, which is due to the replacement of smaller  $\text{Co}^{2+}$  ions ( $r_{\text{Co}^{2+}} = 0.065\text{ nm}$ ) by larger  $\text{Ni}^{2+}$  ions ( $r_{\text{Ni}^{2+}} = 0.069\text{ nm}$ ) on the metal sites. No secondary phase is observed in these patterns, confirming the obtained samples

with high purity. These suggest that the Ni doped products form solid solutions rather than a simple physical mixture of NiS<sub>2</sub> and CoS<sub>2</sub>.



**Figure 2.** (a) XRD patterns of Ni<sub>x</sub>Co<sub>1-x</sub>S<sub>2</sub> and (b) the partial magnification of the (200) peaks between 30.5~33.5°

The SEM images of Ni<sub>x</sub>Co<sub>1-x</sub>S<sub>2</sub> with  $x$  from 0 to 1 are exhibited in Figure 3a-e. All samples show large secondary particles with sphere-like structures, which are formed by the agglomeration of nano-sized primary particles. The size of the primary particles first decreases and then increases as the Ni ratio rises. The Ni<sub>0.5</sub>Co<sub>0.5</sub>S<sub>2</sub> sample shows the smallest primary particle size, which may be helpful in exposing more active sites. Co and Ni contents in the Ni<sub>x</sub>Co<sub>1-x</sub>S<sub>2</sub> ( $x = 0.25, 0.5, 0.75$ ) were confirmed by ICP, and the results are displayed in Figure 3f. As expected, the Ni ratio in Ni<sub>x</sub>Co<sub>1-x</sub>S<sub>2</sub> samples likewise steadily increases with increasing Ni amount. It seems that the content of Co is somewhat higher than the corresponding designed ratio.



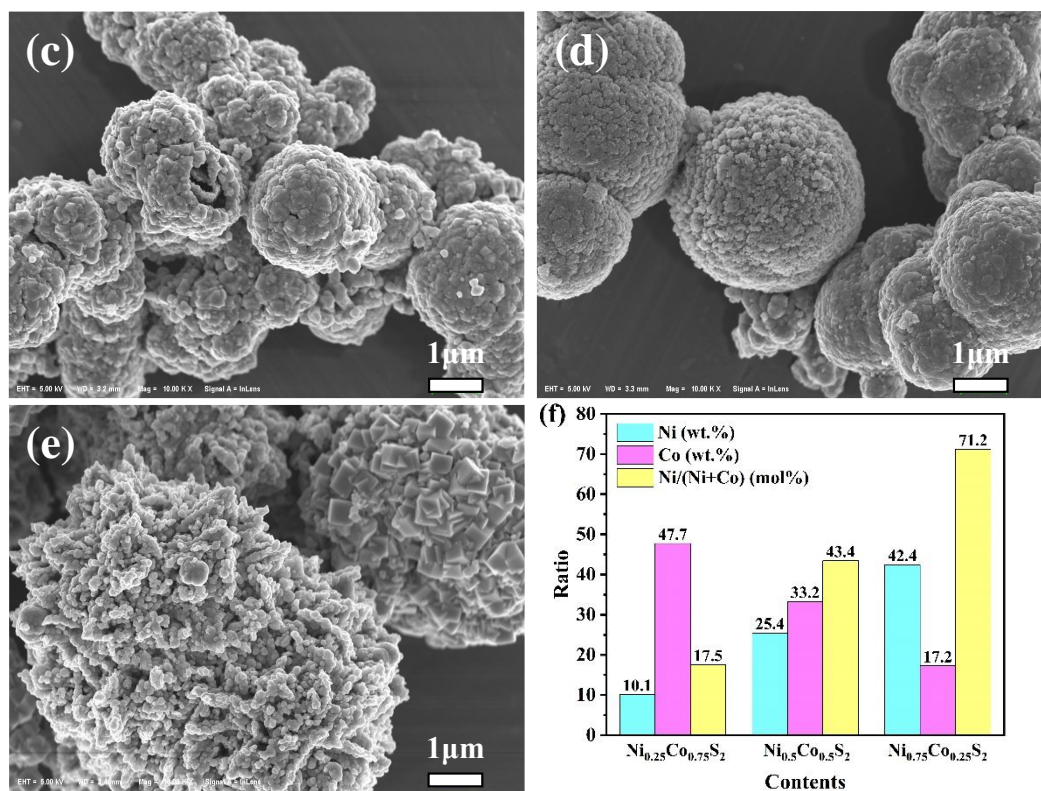


**Figure 3.** SEM images of (a) CoS<sub>2</sub>, (b) Ni<sub>0.25</sub>Co<sub>0.75</sub>S<sub>2</sub>, (c) Ni<sub>0.5</sub>Co<sub>0.5</sub>S<sub>2</sub>, (d) Ni<sub>0.75</sub>Co<sub>0.25</sub>S<sub>2</sub> and (e) NiS<sub>2</sub>. (f) ICP results of Ni<sub>x</sub>Co<sub>1-x</sub>S<sub>2</sub> (x = 0.25, 0.5, and 0.75)

The surface chemical states of CoS<sub>2</sub>, Ni<sub>0.5</sub>Co<sub>0.5</sub>S<sub>2</sub> and NiS<sub>2</sub> were analyzed by XPS. Figure 4a proclaims the existence of Ni, Co and S elements in Ni<sub>0.5</sub>Co<sub>0.5</sub>S<sub>2</sub> with a molar ratio of 1: 1.3: 4.4, which is consistent with the ICP result. Furthermore, C element in the spectrum is attributed to external contamination, and O element originates from the inevitable surface oxidation. The high-resolution spectra of Co 2p and Ni 2p ( Figure 4b and 4c) show that Co<sup>2+</sup>/Co<sup>3+</sup> and Ni<sup>2+</sup>/Ni<sup>3+</sup> coexist in Ni<sub>0.5</sub>Co<sub>0.5</sub>S<sub>2</sub>, which is consistent with the structure reported in the previous literatures [34, 35]. The Co 2p spectra of Ni<sub>0.5</sub>Co<sub>0.5</sub>S<sub>2</sub> (Figure 4b) can be deconvoluted into Co<sup>3+</sup> and Co<sup>2+</sup> as well as two satellite peaks [36]. Two peaks at 779.3 eV and 780.3 eV are attributed to Co<sup>3+</sup> and Co<sup>2+</sup> 2p<sub>3/2</sub> orbitals, while the peaks at 794.2 eV and 795.1 eV originate from Co<sup>3+</sup> and Co<sup>2+</sup> 2p<sub>1/2</sub> orbitals, respectively. At higher binding energy, 783.6 eV and 799.4 eV, satellite peaks of 2p<sub>3/2</sub> and 2p<sub>1/2</sub> for Co are detected [35].

For the Ni 2p spectra (Figure 4c), the peaks at 854.3 eV and 855.7 eV are due to Ni<sup>2+</sup> and Ni<sup>3+</sup> 2p<sub>3/2</sub> orbits, respectively, while 871.4 eV and 872.8 eV belong to Ni<sup>2+</sup> and Ni<sup>3+</sup> 2p<sub>1/2</sub> orbits, respectively [37]. The two succeeding satellite peaks are also detected at 859.7 eV and 876.8 eV. In Figure 4d, the S 2p spectrum of Ni<sub>0.5</sub>Co<sub>0.5</sub>S<sub>2</sub> can be assigned to three peaks. S 2p<sub>3/2</sub> and S 2p<sub>1/2</sub> of S<sub>2</sub><sup>2-</sup> are responsible for the two main peaks, which locate at 163.3 eV and 164.5 eV, respectively [38]. The subsequent weak peak at 169.5 eV could be identified as an S-O bond, possibly rooting in slight surface oxidization due to the exposure to air [39]. In comparison to CoS<sub>2</sub> and NiS<sub>2</sub>, the binding energies of Co 2p in Ni<sub>0.5</sub>Co<sub>0.5</sub>S<sub>2</sub> show positive shifts, while the binding energies of Ni 2p exhibit negative shifts, implying the synergistic effect between Co ions and Ni ions originate from the electronic interaction in Ni<sub>0.5</sub>Co<sub>0.5</sub>S<sub>2</sub> [31, 40, 41].

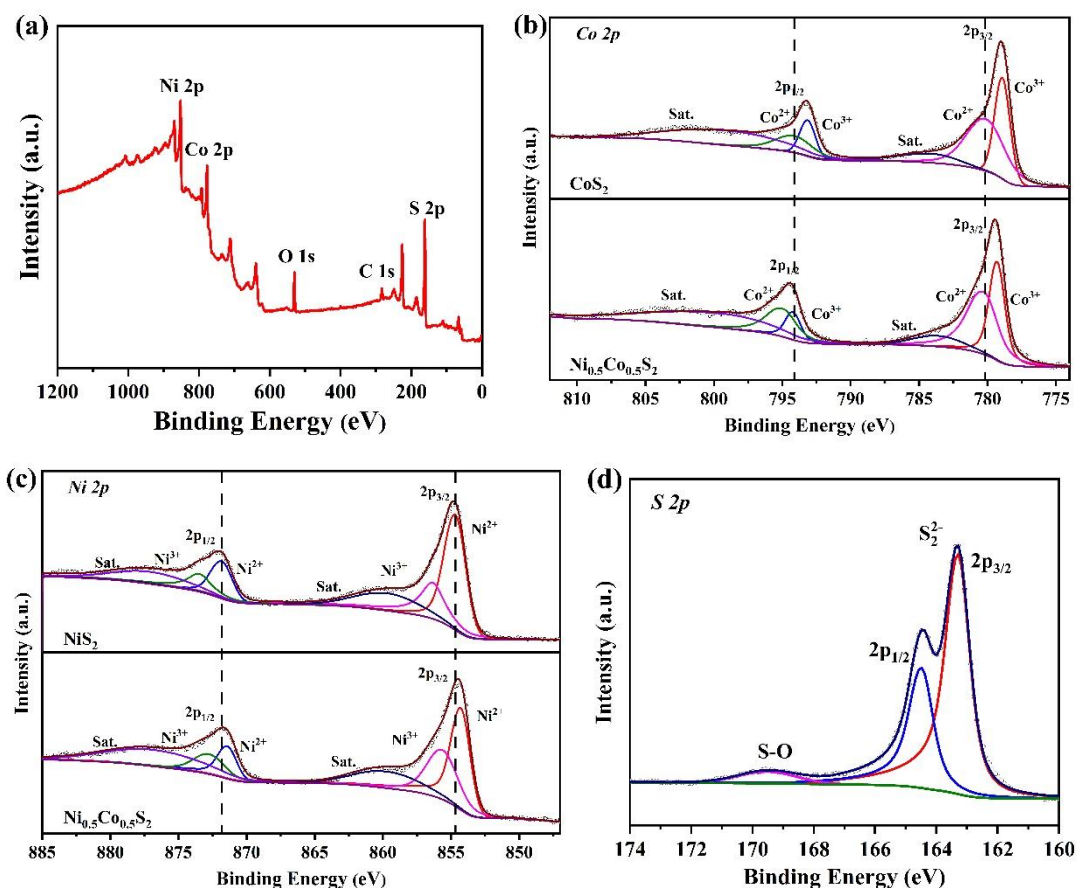


**Figure 4.** (a) The XPS survey spectrum of  $\text{Ni}_{0.5}\text{Co}_{0.5}\text{S}_2$ . The high-resolution spectra of (b) Co 2p for  $\text{CoS}_2$  and  $\text{Ni}_{0.5}\text{Co}_{0.5}\text{S}_2$ , (c) Ni 2p for  $\text{NiS}_2$  and  $\text{Ni}_{0.5}\text{Co}_{0.5}\text{S}_2$  and (d) S 2p for  $\text{Ni}_{0.5}\text{Co}_{0.5}\text{S}_2$

Li-O<sub>2</sub> cells containing  $\text{Ni}_x\text{Co}_{1-x}\text{S}_2$  were assembled to test the electrochemical performances. The CV plots of cells with  $\text{Ni}_x\text{Co}_{1-x}\text{S}_2$  between 2.0~4.5 V (vs.  $\text{Li}^+/\text{Li}$ ) at the scanning rate of 1 mV/s are shown in Figure 5a. All cells show a prominent reduction peak at ~2.4 V during the cathodic scanning due to the generation of the discharge product  $\text{Li}_2\text{O}_2$ . During the anodic scanning, the oxidation peaks at ~3.2 V represent the invertible decomposition of  $\text{Li}_2\text{O}_2$  [42]. It can be found that by doping a certain amount of Ni element, the ORR onset potential and the ORR peak current density of the cells improve at first. The cell with  $\text{Ni}_{0.5}\text{Co}_{0.5}\text{S}_2$  exhibits the highest ORR onset potential, the lowest OER onset potential and the largest reduction peak current density, indicating that  $\text{Ni}_{0.5}\text{Co}_{0.5}\text{S}_2$  owns the best catalytic properties. This may be due to the synergistic effects of the various metal ions, as well as the increased active sites because of the smallest particle size. However, when the Ni content continuously increases, the catalytic performances of the samples reduce, which can be put down to the lower catalytic activity of  $\text{NiS}_2$  and decreased active sites due to larger particle size. Therefore, the doping amount is of great significance in tuning the catalytic activities of the  $\text{Ni}_x\text{Co}_{1-x}\text{S}_2$  catalysts. The initial charge-discharge tests of the cells with  $\text{Ni}_x\text{Co}_{1-x}\text{S}_2$  were carried out between 2.0~4.5 V at 100 mA/g (see Figure 5b). With increasing Ni contents, the discharge capacities of the cells increase firstly and then progressively decrease. The discharge capacity of the cell with  $\text{Ni}_{0.5}\text{Co}_{0.5}\text{S}_2$  is up to 4878 mAh/g, which is higher than those of the cells with  $\text{CoS}_2$  (3530 mAh/g),  $\text{Ni}_{0.25}\text{Co}_{0.75}\text{S}_2$  (3663 mAh/g),

$\text{Ni}_{0.75}\text{Co}_{0.25}\text{S}_2$  (3919 mAh/g) and  $\text{NiS}_2$  (3278 mAh/g). Obviously, the cells with bimetallic catalysts reveal higher discharge specific capacities than those with monometallic catalysts, which might contribute to the enhanced catalytic activities of the bimetallic sulfides. Compared with some reported metal oxides and carbon based materials [43-46], the  $\text{Ni}_{0.5}\text{Co}_{0.5}\text{S}_2$  exhibits stronger competitiveness in enhancing the discharge/charge capacities.

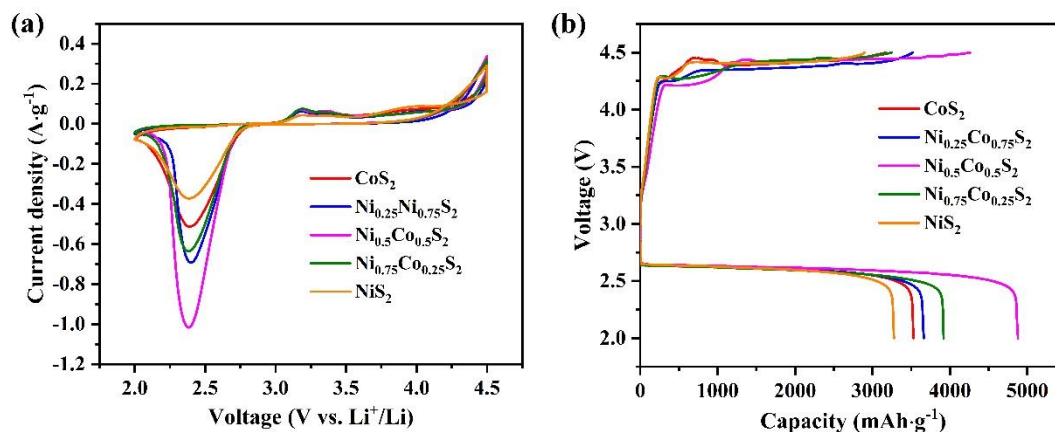


**Figure 5.** (a) CV curves and (b) the initial discharge-charge curves of the cells with  $\text{Ni}_x\text{Co}_{1-x}\text{S}_2$  at 100 mA/g

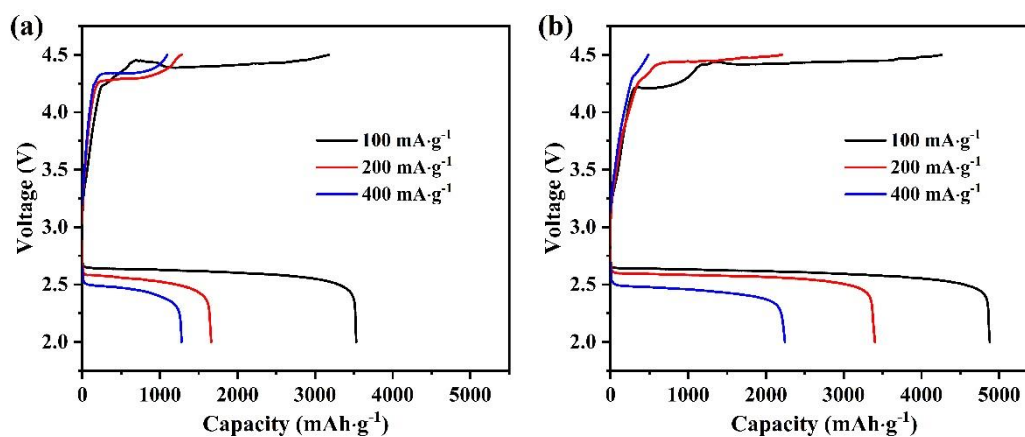


**Figure 6.** First discharge-charge curves of the cells with (a)  $\text{CoS}_2$  and (b)  $\text{Ni}_{0.5}\text{Co}_{0.5}\text{S}_2$  at current densities of 100, 200, 400 mA/g

Figure 6 exhibits the rate performances of two representative cells at 100, 200 and 400 mA/g. The cell with  $\text{CoS}_2$  reveals an initial capacity of 3530 mAh/g at 100 mA/g, which significantly decreases to 1662 mAh/g and 1279 mAh/g at increasing current densities of 200 mA/g and 400 mA/g, respectively. However, the cell with  $\text{Ni}_{0.5}\text{Co}_{0.5}\text{S}_2$  shows the initial discharge specific capacities of 4878, 3400 and 2244 mAh/g at 100, 200 and 400 mA/g, respectively. The discharge capacities of the cell with  $\text{Ni}_{0.5}\text{Co}_{0.5}\text{S}_2$  are attenuated by 30.3% and 54.0% at higher current densities. Nevertheless, the discharge capacity reduction of the cell with  $\text{CoS}_2$  is 52.9% and 63.8%. These suggest that the

$\text{Ni}_{0.5}\text{Co}_{0.5}\text{S}_2$  promotes the reaction kinetics of lithium-oxygen cell compare with  $\text{CoS}_2$ , which benefits from the improvement of the catalytic performances of  $\text{CoS}_2$  by Ni doping.

The cycling stabilities of the cells with  $\text{CoS}_2$  and  $\text{Ni}_{0.5}\text{Co}_{0.5}\text{S}_2$  at a limited capacity of 500 mAh/g under 100 mA/g are displayed in Figure 7. As shown in Figure 7a and 7b, the cells with  $\text{CoS}_2$  and  $\text{Ni}_{0.5}\text{Co}_{0.5}\text{S}_2$  show similar discharge curves with a voltage plateau around 2.7 V. The cycle number of the cell with  $\text{Ni}_{0.5}\text{Co}_{0.5}\text{S}_2$  can reach up to 67 times before the discharge terminal voltage falls down to 2.0 V, which is 27 times higher than that of the cell with  $\text{CoS}_2$ . Figure 7c reveals the profiles of the discharge and charge terminal voltages of the cells with  $\text{CoS}_2$  and  $\text{Ni}_{0.5}\text{Co}_{0.5}\text{S}_2$  during cycling. Obviously, more stable changes in charge and discharge terminal voltages could be observed in the cell with  $\text{Ni}_{0.5}\text{Co}_{0.5}\text{S}_2$ , suggesting that the  $\text{Ni}_{0.5}\text{Co}_{0.5}\text{S}_2$  improves the cycling stabilities of the cell. Here, Ni doping involves in enhancing the cycling performance of the cell, which may be due to the fact that bimetallic disulfides with better catalytic activity promote the redox reactions. For comparison, the cycling performances of the LOBs containing  $\text{Ni}_{0.5}\text{Co}_{0.5}\text{S}_2$  in this work and various cathode catalysts in some previous literatures have been listed in Table 1. As listed, superior cycling performance of LOB can be achieved by using  $\text{Ni}_{0.5}\text{Co}_{0.5}\text{S}_2$ , inferring the development of bimetallic sulfides is a potential strategy to promote the electrochemical performances of LOBs.

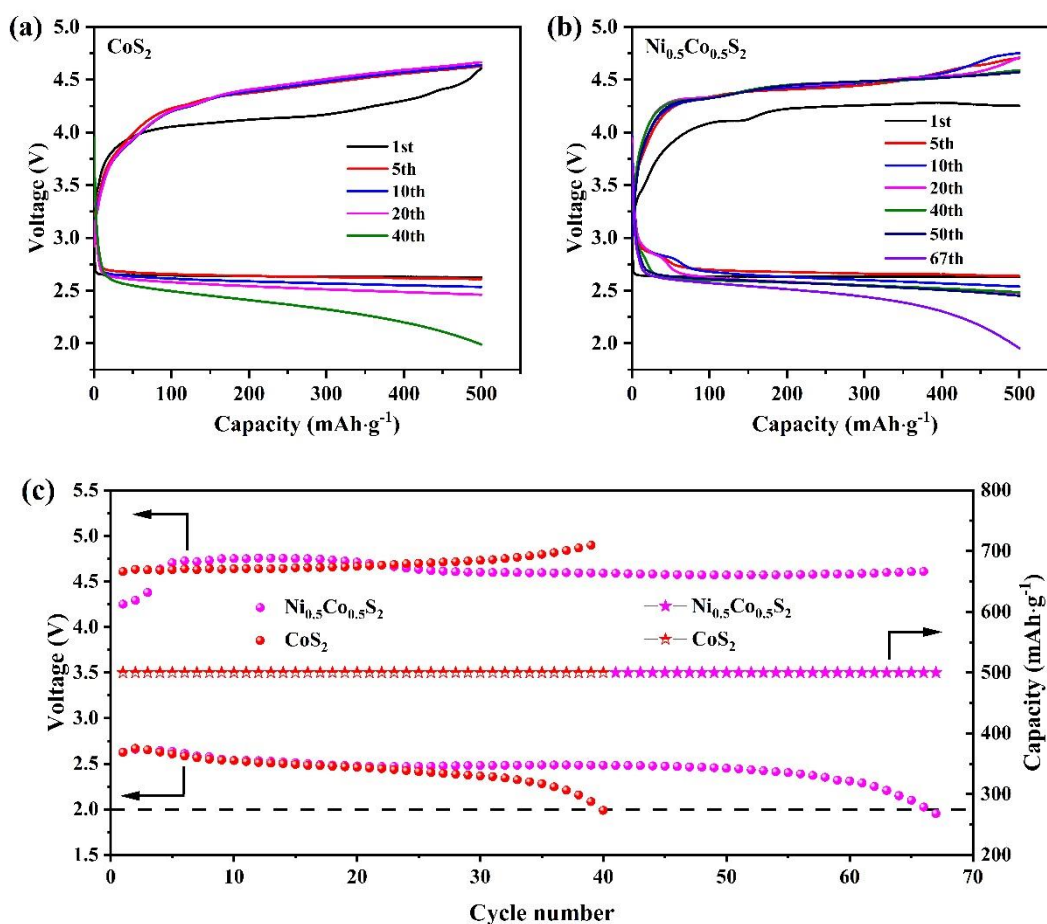


**Figure 7.** Cycling performances of the cells with  $\text{CoS}_2$  and  $\text{Ni}_{0.5}\text{Co}_{0.5}\text{S}_2$  under 100 mA/g at a limited charge-discharge capacity of 500 mAh/g

**Table 1.** The cycling performances of the LOBs in this work and in some previous literatures.

Cathode Catalysts	Current Density	Limited Capacity	Cycling Performance (Cycles)	Ref.
MoS <sub>2</sub>	0.1 mA/cm <sup>2</sup>	500 mAh/g	50	12
CoS <sub>2</sub> /CNT	0.05 mA/cm <sup>2</sup>	500 mAh/g	52	20
NiS	75 mA/g	900 mAh/g	30	22
CoS <sub>2</sub> /RGO	200 mA/g	500 mAh/g	20	47
Co <sub>3</sub> S <sub>4</sub>	100 mA/g	500 mAh/g	25	48
MoS <sub>x</sub> /HRG	0.1 mA/cm <sup>2</sup>	500 mAh/g	30	49
RuO <sub>2</sub> /MoS <sub>2</sub>	300 mA/g	1000 mAh/g	45	50
Ni <sub>0.5</sub> Co <sub>0.5</sub> S <sub>2</sub>	100 mA/g	500 mAh/g	67	This work

#### 4. CONCLUSIONS

In summary, we have successfully synthesized Ni<sub>x</sub>Co<sub>1-x</sub>S<sub>2</sub> nano-particles as electrocatalysts. Among the prepared samples, Ni<sub>0.5</sub>Co<sub>0.5</sub>S<sub>2</sub> owns the best catalytic properties, which promote the electrochemical performances of the LOBs. The cell with Ni<sub>0.5</sub>Co<sub>0.5</sub>S<sub>2</sub> presents an initial capacity of 4878 mAh/g at 100 mA/g, which are obviously higher than those of other cells. Moreover, the cell containing Ni<sub>0.5</sub>Co<sub>0.5</sub>S<sub>2</sub> also shows higher specific capacities compare with that containing CoS<sub>2</sub> at elevated current densities of 200 mA/g and 400 mA/g. Superior cycling performance is also attained in the cell with Ni<sub>0.5</sub>Co<sub>0.5</sub>S<sub>2</sub>, in which the cycling numbers increase by 67.5% compare with the cell containing CoS<sub>2</sub> with a limited capacity of 500 mAh/g at 100 mA/g. The enhanced catalytic activities are primarily attributed to the synergistic catalytic effect, ensuring its encouraging applications for lithium-oxygen batteries.

#### ACKNOWLEDGEMENTS

This work was supported by Natural Science Foundation of China (No. 51790490).

#### References

1. X. Chi, M. Li, J. Di, P. Bai, L. Song, X. Wang, F. Li, S. Liang, J. Xu, J. Yu, *Nature*, 592 (2021)551.
2. T.L. Kulova, V.N. Fateev, E.A. Seregina, A.S. Grigoriev, *Int. J. Electrochem. Sci.*, 15 (2020) 7242.
3. J. Li, L.F. Hou, L.H. Luan, T.Y. Zhang, H. Sun, *Int. J. Electrochem. Sci.*, 16 (2021) 210749.

4. D. Yu, Y. Ma, F. Hu, C.C. Lin, L. Li, H.Y. Chen, X. Han, S. Peng, *Adv. Energy Mater.*, 11 (2021) 2101242.
5. W.J. Kwak, Rosy, D. Sharon, C. Xia, H. Kim, L.R. Johnson, P.G. Bruce, L.F. Nazar, Y.K. Sun, A.A. Frimer, M. Noked, S.A. Freunberger, D. Aurbach, *Chem. Rev.*, 120 (2020) 6626.
6. C. Li, H. Liu, Z. Yu, *Appl. Catal. B-Environ.*, 241 (2019) 95.
7. Z.F. Huang, J. Wang, Y. Peng, C.Y. Jung, A. Fisher, X. Wang, *Adv. Energy Mater.*, 7 (2017) 1700544.
8. V. Rai, K.P. Lee, D. Safanama, S. Adams, D.J. Blackwood, *ACS Appl. Energ. Mater.*, 3 (2020) 9417.
9. Y.J. Wang, B. Fang, D. Zhang, A. Li, D.P. Wilkinson, A. Ignaszak, L. Zhang, J. Zhang, *Electrochem. Energy Rev.*, 1 (2018) 1.
10. J. Zhu, M. Xie, Z. Chen, Z. Lyu, M. Chi, W. Jin, Y. Xia, *Adv. Energy Mater.*, 10 (2020) 1904114.
11. M.D. Bhatt, J.Y. Lee, *Energy Fuels*, 34 (2020) 6634.
12. M. Asadi, B. Kumar, C. Liu, P. Phillips, P. Yasaei, A. Behranginia, P. Zapol, R.F. Klie, L.A. Curtiss, A. Salehi-Khojin, *ACS Nano*, 10 (2016) 2167.
13. H. Fang, T. Huang, J. Mao, S. Yao, M.M. Dinesh, Y. Sun, D. Liang, L. Qi, J. Yu, Z. Jiang, *ChemistrySelect*, 3 (2018) 10418.
14. K. Marcus, K. Liang, W. Niu, Y. Yang, *J Phys Chem Lett*, 9 (2018) 2746.
15. V. Urbanova, P. Lazar, N. Antonatos, Z. Sofer, M. Otyepka, M. Pumera, *ACS Appl. Mater. Interfaces*, 12 (2020) 20383.
16. J. Zhang, Y. Liu, B. Xia, C. Sun, Y. Liu, P. Liu, D. Gao, *Electrochim. Acta*, 259 (2018) 955.
17. G. Chen, H. Li, Y. Zhou, C. Cai, K. Liu, J. Hu, H. Li, J. Fu, M. Liu, *Nanoscale*, 13 (2021) 13604.
18. X. Cui, Z. Xie, Y. Wang, *Nanoscale*, 8 (2016) 11984.
19. S. Vijaya, G. Landi, J.J. Wu, S. Anandan, *J. Power Sources*, 478 (2020) 229068.
20. X. Lin, T. Zhang, C. Chu, Z. Li, R. Liu, P. Li, Y. Li, Z. Huang, Y. Ma, *ACS Sustain. Chem. Eng.*, 8 (2020) 7581.
21. Y. Seon Kim, G.H. Lee, B. Ju, D.W. Kim, *Chem. Eng. J.*, 418 (2021) 129367.
22. Z. Ma, X. Yuan, Z. Zhang, D. Mei, L. Li, Z.F. Ma, L. Zhang, J. Yang, J. Zhang, *Sci Rep*, 5 (2015) 18199.
23. Q. Wang, X. Wang, H. He, *J. Power Sources*, 448 (2020) 227397.
24. B. Ju, H.J. Song, G.H. Lee, M.C. Sung, D.W. Kim, *Energy Storage Mater.*, 24 (2020) 594.
25. W. Zhu, X. Yue, W. Zhang, S. Yu, Y. Zhang, J. Wang, J. Wang, *Chem. Commun.*, 52 (2016) 1485.
26. T. Tian, L. Huang, L. Ai, J. Jiang, *J. Mater. Chem. A*, 5 (2017) 20985.
27. T. Huang, H. Fang, L. Xu, Z. Wang, Y. Xin, J. Yu, S. Yao, Z. Zhang, *J. Catal.*, 359 (2018) 223.
28. W. Peng, A. Deshmukh, N. Chen, Z. Lv, S. Zhao, J. Li, B. Yan, X. Gao, L. Shang, Y. Gong, L. Wu, M. Chen, T. Zhang, H. Gou, *ACS Catal.*, 12 (2022) 3743.
29. G. Fu, J.M. Lee, *J. Mater. Chem. A*, 7 (2019) 9386.
30. D. Chinnadurai, R. Rajendiran, P. Kandasamy, *J. Colloid Interface Sci.*, 606 (2022) 101.
31. Y. Wu, Z. Yu, H. Liu, K. Chen, F. Zhao, Y. Cao, *Funct. Mater. Lett.*, 13 (2020) 2051015.
32. M. Xu, X. Hou, X. Yu, Z.F. Ma, J. Yang, X. Yuan, *J. Electrochem. Soc.*, 166 (2019) F406.
33. A. Hu, J. Long, C. Shu, C. Xu, T. Yang, R. Liang, J. Li, *Electrochim. Acta*, 301 (2019) 69.
34. Z. Peng, D. Jia, A.M. Al-Enizi, A.A. Elzatahry, G. Zheng, *Adv. Energy Mater.*, 5 (2015) 1402031.
35. G. He, W. Zhang, Y. Deng, C. Zhong, W. Hu, X. Han, *Catalysts*, 7 (2017) 366.
36. Z. Xie, H. Tang, Y. Wang, *ChemElectroChem*, 6 (2019) 1206.
37. H. Guo, L. Tang, Q. Tian, Y. Chu, B. Shi, X. Yin, H. Huo, X. Han, C. Yang, C. Wang, K. Tang, C. Wang, X. Zhang, J. Wang, L. Kong, Z. Lu, *ACS Appl. Mater. Interfaces*, 12 (2020) 50377.
38. J. Zhang, X. Bai, T. Wang, W. Xiao, P. Xi, J. Wang, D. Gao, J. Wang, *Nano-Micro Lett.*, 11 (2019) 2.
39. A. Sumboja, J. Chen, Y. Ma, Y. Xu, Y. Zong, P.S. Lee, Z. Liu, *ChemCatChem*, 11 (2019) 1205.

40. L. Zhu, D. Susac, M. Teo, K. Wong, P. Wong, R. Parsons, D. Bizzotto, K. Mitchell, S. Campbell, *J. Catal.*, 258 (2008) 235.
41. X. Zhang, P. Li, B. Xu, J. Wang, G. Fan, X. Zhang, X. Liu, K. Zhang, W. Jiang, *Ind. Eng. Chem. Res.*, 60 (2021) 8312.
42. P. Zhang, Z. Wang, P. Wang, X. Hui, D. Zhao, Z. Zhang, L. Yin, *ACS Appl. Energ. Mater.*, 5 (2022) 3359.
43. M. He, P. Zhang, S. Xu, X. Yan, *ACS Appl. Mater. Interfaces*, 8 (2016) 23713.
44. L. Liu, Y. Hou, J. Wang, J. Chen, H.K. Liu, Y. Wu, J. Wang, *Adv. Mater. Interfaces*, 3 (2016) 1600030.
45. D. Cao, Q. Wang, X. Yin, Y. Sun, M. Ma, Y. Wu, X. Liu, *Energy Fuels*, 34 (2020) 10225.
46. L. Liu, T. Ma, W. Fang, Y. Liu, K. Konstantinov, J. Wang, H. K. Liu, *Energy Environ. Mater.*, 4 (2021) 239.
47. Z. Lyu, J. Zhang, L. Wang, K. Yuan, Y. Luan, P. Xiao, W. Chen, *RSC Adv.*, 6 (2016) 31739.
48. P. Sennu, M. Christy, V. Aravindan, Y.G. Lee, K. S. Nahm, Y.S. Lee, *Chem. Mater.*, 27 (2015) 5726.
49. L. Li, C. Chen, J. Su, P. Kuang, C. Zhang, Y. Yao, T. Huang, A. Yu, *J. Mater. Chem. A*, 4 (2016) 10986.
50. Y. S. Jeong, Y. J. Jang, S. J. Park, Y. J. Lee, *Bull. Korean Chem. Soc.*, 40 (2019) 642.

© 2022 The Authors. Published by ESG ([www.electrochemsci.org](http://www.electrochemsci.org)). This article is an open access article distributed under the terms and conditions of the Creative Commons Attribution license (<http://creativecommons.org/licenses/by/4.0/>).